

# Nondestructive *In Situ* Identification of Crystal Orientation of Anisotropic ZnO Nanostructures

Srikanth Singamaneni,<sup>†</sup> Maneesh Gupta,<sup>†</sup> Rusen Yang,<sup>†</sup> Melanie M. Tomczak,<sup>‡</sup> Rajesh R. Naik,<sup>‡</sup> Zhong L. Wang,<sup>†</sup> and Vladimir V. Tsukruk<sup>†,\*</sup>

<sup>†</sup>School of Materials Science and Engineering, Georgia Institute of Technology, Atlanta, Georgia 30318, and <sup>‡</sup>Air Force Research Laboratory, Materials and Manufacturing Directorate, Wright-Patterson AFB, Dayton, Ohio 45433

One-dimensional nano- and microstructures such as wires, rods, belts, and tubes of various metals and semiconductors have attracted increased attention owing to their unique mechanical, electrical, and optical properties compared to their bulk counterparts.<sup>1–4</sup> Important materials such as ZnO, GaN, ZnS, and CdSe utilized for fabrication of one-dimensional nanostructures belong to the wurtzite family. These materials are utilized in numerous fields such as optoelectronics, lasing, and piezoelectric devices.<sup>5–14</sup> Owing to the unique combination of the semiconducting and piezoelectric properties of ZnO nanostructures, a variety of novel devices have been fabricated for applications such as nanogenerators, piezoelectric diodes, field effect transistors, and thermal and chemical sensors.<sup>15–19</sup>

The electrical and optical properties of nanostructures critically depend on their composition, crystalline structure, and orientation, and thus these parameters must be known for nanostructures integrated into nanodevices. To this end, X-ray analysis is frequently used for probing the crystallinity and lattice dimensions of relatively large quantities of nanostructures, but it is not applicable for probing the crystalline orientation of an individual nanostructure. On the other hand, transmission electron microscopy (TEM) and electron diffraction have been the primary tool for identifying the growth direction and crystal facets of individual ZnO nanowires and nanobelts.<sup>20</sup> However, TEM requires special sample preparation and cannot be applied to nanostructures packaged in their respective devices. Therefore, a fast, unambiguous, and nondestructive technique for identification of the crystalline orientation of wurtzite ma-

**ABSTRACT** We present a novel method for direct, fast, nonambiguous, and nondestructive identification of the growth direction and orientation of *individual* ZnO nanostructures in the device-ready environment by exploiting high-resolution confocal Raman mapping. Various features of the Raman spectrum of ZnO nanostructures, vapor deposition grown nanobelts and peptide-assisted vertical nanorods, were found to be sensitive to the relative orientation of the crystal plane. Furthermore, we discovered that the waveguiding property of the ZnO nanobelt is also orientation dependent and results in either apparent enhancement or suppression of Raman scattering from the underlying substrate. We demonstrate that various features of Raman spectrum of ZnO and the modulation of the substrate signal can be employed for the rapid and nondestructive identification of the crystal growth direction and orientation of these nanostructures even after integration into devices, which is impossible with current electron microscopy and diffraction techniques. We believe that the general features observed here are equally applicable to other wurtzite nanostructures (ZnS, GaN) which are critical in optoelectronics, lasing, and piezotronic applications.

**KEYWORDS:** ZnO nanostructure · polarized Raman · bioenabled growth · waveguiding · crystal plane

terials and nanostructures in the device environment is extremely useful for the development and testing of devices for new applications.

As known, Raman scattering is an excellent nondestructive tool to probe the chemical composition, physical state, phonon confinement, and lattice dynamics of various organic and inorganic materials. For example, Raman spectroscopy has been extensively employed for probing the diameter, chirality, alignment, stress, and deformation in carbon nanotubes and other nanostructures.<sup>21–27</sup> Very recently, it has been demonstrated that confocal Raman spectroscopy can be employed to obtain information on the phase, growth direction, and radial crystallographic orientation of GaN nanowires.<sup>28,29</sup> The E<sub>2</sub> band of ZnO has been demonstrated to be highly sensitive to internal stress in the crystalline structure.<sup>30</sup> The shift of the E<sub>2</sub> band to high frequencies has been employed to monitor

\*Address correspondence to vladimir@mse.gatech.edu.

Received for review June 27, 2009 and accepted July 29, 2009.

Published online August 5, 2009.  
10.1021/nn900687g CCC: \$40.75

© 2009 American Chemical Society

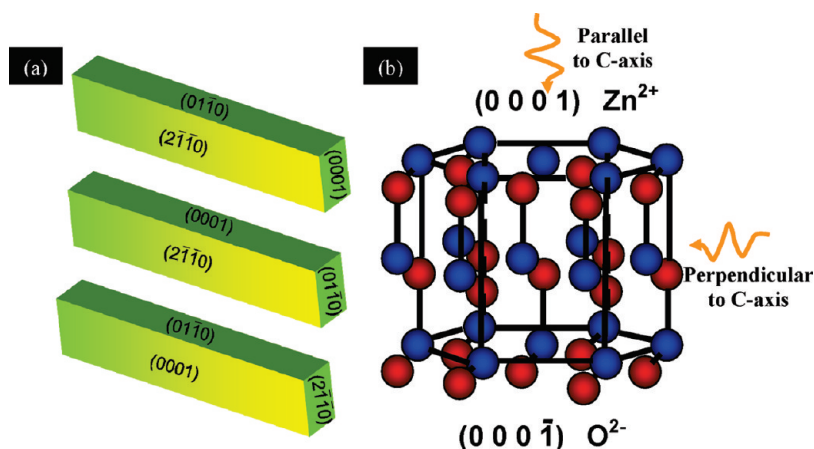


Figure 1. (a) Schematic showing the various possible growth orientations of the ZnO nanobelts. (b) Schematic of the crystal structure of the ZnO showing the tetrahedrally coordinated alternating planes of  $\text{Zn}^{2+}$  and  $\text{O}^{2-}$ .

the stress state in vertically grown ZnO nanorods of various diameters.<sup>31</sup>

In the present work, confocal Raman microscopy was employed to identify the growth orientation (*c*-axis) of one-dimensional ZnO nanostructures, a popular representative of wurtzite nanomaterials. Different Raman modes, based on selection rules, in conjunction with electron diffraction were used to unambiguously identify the crystal planes. Furthermore, waveguiding properties of ZnO nanostructures result in the suppression of the Raman scattering from the substrate in cer-

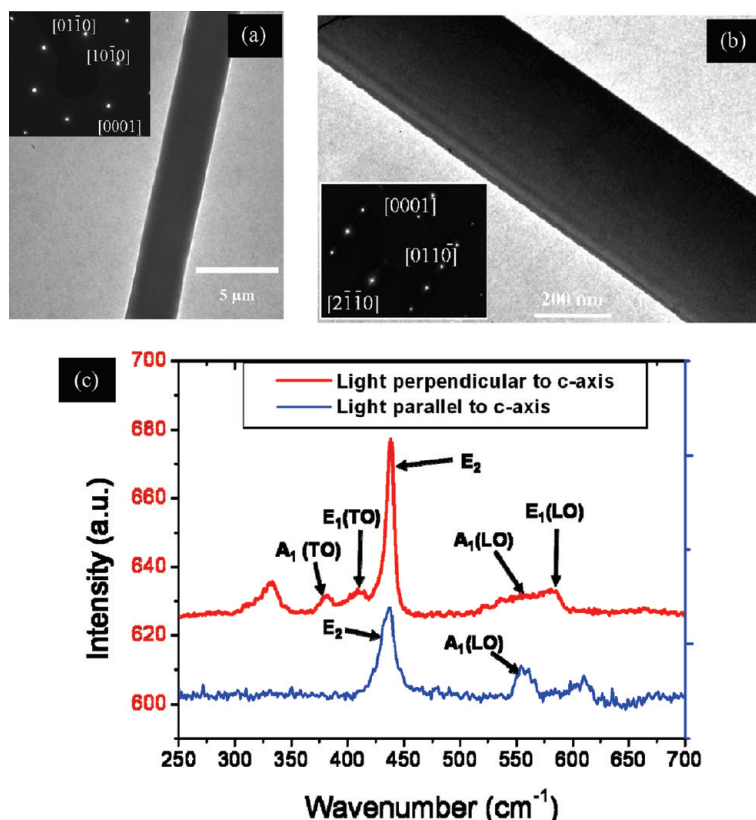


Figure 2. (a,b) TEM images of the ZnO nanobelt with the electron diffraction pattern. (c) Raman spectra obtained from ZnO nanobelts with *c*-axis parallel (blue) and perpendicular (red) to incident light.

tain directions and enhancement in the other directions. We demonstrate that this unique feature discovered here can be exploited to easily identify various crystal planes and waveguiding properties of ZnO nanostructures in a completely non-destructive manner. To our knowledge, high-resolution confocal Raman mapping of individual ZnO nanostructures and nanodevices with unambiguous identification of crystal orientation has not been reported to date. Furthermore, the modulation of the substrate Raman scattering signal depending on the crystal plane orientation of the nanostructure has never been observed.

## RESULTS AND DISCUSSION

In this paper, we will primarily focus on ZnO nanobelts and nanorods of two different types, although the general features can be extended to any nanostructure with wurtzite crystal structure. Two one-dimensional structures investigated here are nanobelts grown by vapor deposition and vertical nanorods using peptide-assisted method (see Experimental Section for growth details).

As known, ZnO (wurtzite) exhibits a hexagonal structure belonging to  $C6mc$  space group.<sup>32</sup> The ZnO structure comprises alternating planes of tetrahedrally coordinated  $\text{O}^{2-}$  and  $\text{Zn}^{2+}$  ions, stacked alternately along the *c*-axis, as schematically shown in Figure 1a. One important feature of ZnO is the polar surfaces, with the most common polar surface being the basal plane. The oppositely charged  $\text{Zn}^{2+}$  and  $\text{O}^{2-}$  ions produce positively charged (0001) and negatively charged (000 $\bar{1}$ ) surfaces, respectively. In the simplest example of a ZnO nanobelt, the fast growth direction can be either  $[2\bar{1}\bar{1}0]$ ,  $[01\bar{1}0]$ , or  $[0001]$ .<sup>32–34</sup>

Wurtzite ZnO structure with four atoms in the unit cell has a total of 12 phonon modes (one LA, two TA, three LO, and six TO branches). The optical phonons at the  $\Gamma$  point of the Brillouin zone in their irreducible representation belong to  $A_1$  and  $E_1$  branches that are both Raman and infrared active, the two non-polar  $E_2$  branches are Raman active only, and the  $B_1$  branches are inactive (silent modes). Furthermore, the  $A_1$  and  $E_1$  modes are each split into LO and TO components with different frequencies. For the  $A_1$  and  $E_1$  mode lattice vibrations, the atoms move parallel and perpendicular to the *c*-axis, respectively. On other hand,  $E_2$  modes are due to the vibration of only the Zn sublattice ( $E_2$ -low) or O sublattice ( $E_2$ -high). The expected Raman peaks for bulk ZnO are at

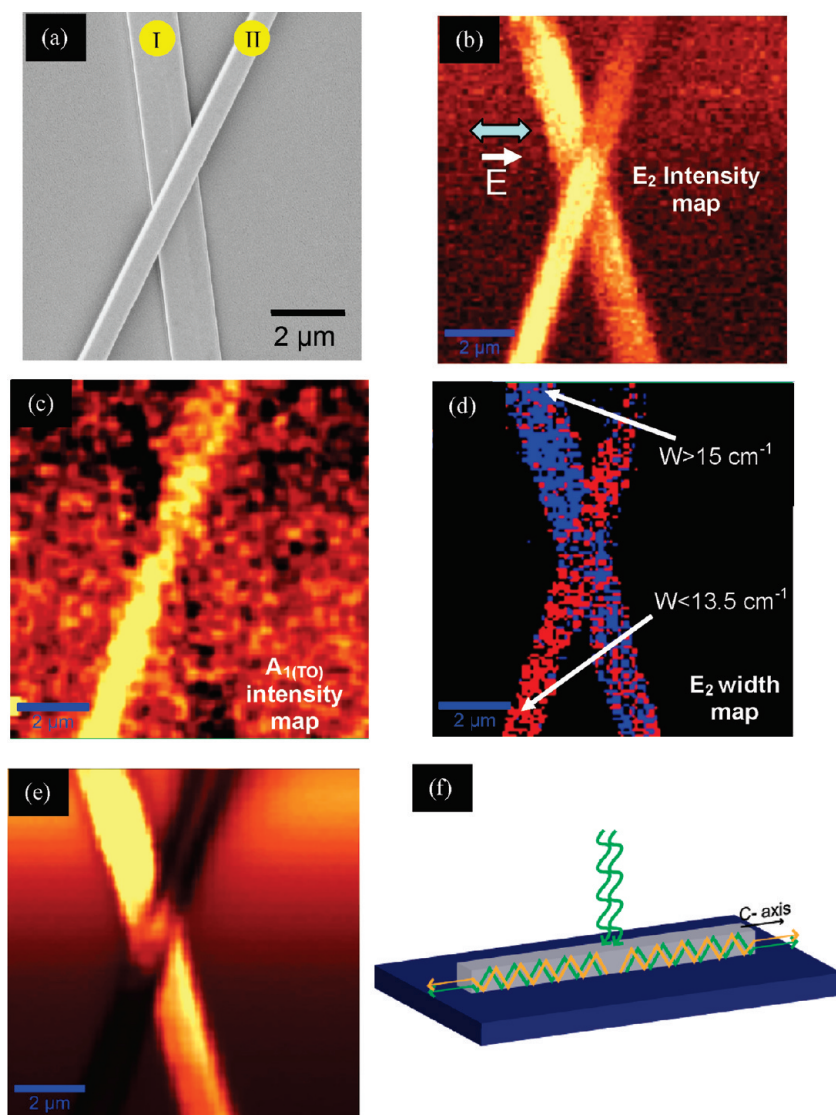


**Figure 3.** (a) SEM image of two intersected ZnO nanobelts. Raman intensity map of two nanobelts shown in (a): (b)  $E_2$  mode, (c)  $A_1(\text{TO})$  mode. (d) Boolean map of the full width at the half-maximum of the  $E_2$  mode, (e) intensity map of the silicon signal at  $520\text{ cm}^{-1}$  showing the modulation in different belts. (f) Schematic showing the waveguiding of the Raman scattered light from the substrate along the  $c$ -axis.

$101\text{ cm}^{-1}$  ( $E_2$ -low),  $380\text{ cm}^{-1}$  ( $A_1$ -TO),  $407\text{ cm}^{-1}$  ( $E_1$ -TO),  $437\text{ cm}^{-1}$  ( $E_2$ -high), and  $583\text{ cm}^{-1}$  ( $E_1$ -LO).

Figure 2a,b shows the TEM images and the corresponding electron diffraction pattern of two different ZnO nanobelts. As can be inferred from the diffraction pattern, the ZnO belt in Figure 2a has the (0001) or (000 $\bar{1}$ ) as the top and bottom large facets, in other words, the growth direction in a non- $c$ -axis direction. On the other hand, the growth direction of the belt shown in the Figure 2b is along the  $c$ -axis. Raman spectra were obtained from these two nanobelts in back scattering geometry, as described in the Experimental Section (Figure 2c). Owing to the orientation of the  $c$ -axis ((0001) plane) relative to the incident source light, the Raman spectra of the nanobelts exhibit distinct features which can be used to identify the relative orientation of the nanobelt facets. Indeed, in accordance with the Raman selection rules, the Raman spectrum of the

ZnO belt with the  $c$ -axis parallel to the incident light (as shown in Figure 1b) exhibits two primary bands, namely,  $E_2$  ( $438\text{ cm}^{-1}$ ) and  $A_1(\text{LO})$  ( $615\text{ cm}^{-1}$ ).<sup>32</sup> For the belt with the  $c$ -axis perpendicular to the incident light (as shown in Figure 1b), the Raman spectrum comprises  $E_2$  ( $438\text{ cm}^{-1}$ ),  $A_1(\text{TO})$  ( $380\text{ cm}^{-1}$ ),  $E_1(\text{TO})$  ( $410\text{ cm}^{-1}$ ),  $A_1(\text{LO})$  ( $615\text{ cm}^{-1}$ ), and  $E_1(\text{LO})$  ( $583\text{ cm}^{-1}$ ) bands.

With the above knowledge, confocal Raman microscopy was performed on the nanobelts (I and II) crossing each other, as shown in Figure 3a. The intensity of the  $E_2$  band (integrated between  $420$  and  $450\text{ cm}^{-1}$ ) of the ZnO nanobelts remains constant along the length of the belts (Figure 3b). A map of the intensity of the  $A_1(\text{TO})$  band shows high intensity for one nanobelt II, while the Raman signal from the other nanobelt I shows no sign of this mode (Figure 3c). From the  $A_1(\text{TO})$  intensity map, it is clear that the nanobelt II has the  $c$ -axis parallel to the substrate, while the  $c$ -axis of the

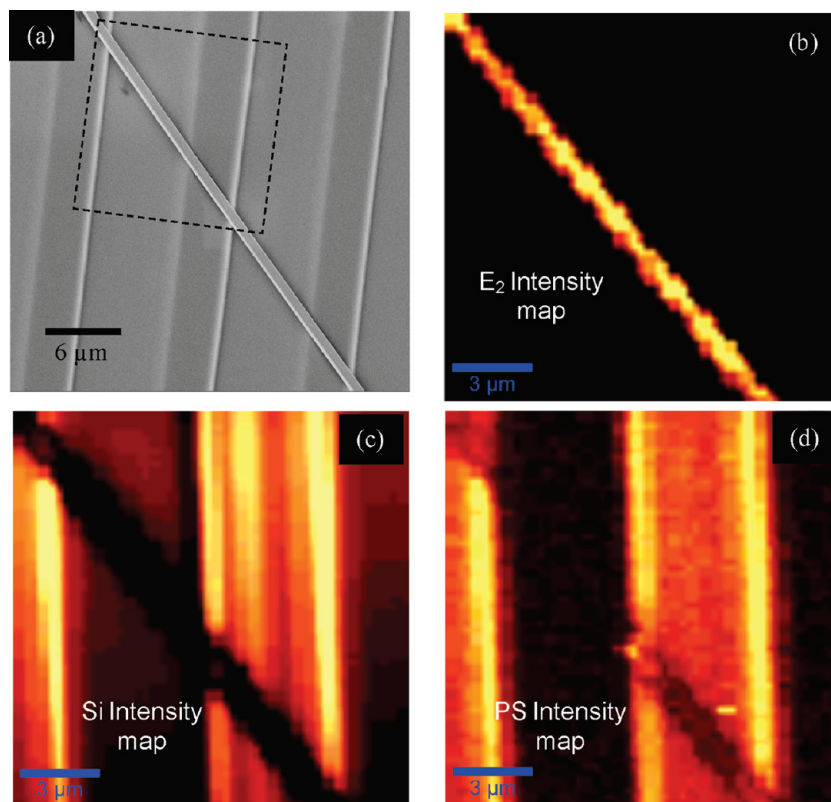


**Figure 4.** (a) SEM image of the nanobelt transferred onto patterned arrays of polystyrene stripes on silicon. Intensity map of (b)  $E_2$  mode of the ZnO nanobelt, (c)  $520\text{ cm}^{-1}$  band of the silicon substrate. (d) Raman band from polystyrene.

nanobelt-I is perpendicular to the substrate. A  $90^\circ$  change in the polarization vector did not result in any noticeable change in the observed features.

The width of the  $E_2$  band was also found to be sensitive to the orientation of the  $c$ -axis of the nanobelt. A Boolean map of the full width at the half-maximum (FWHM) of the  $E_2$  band shows that the two nanobelts can be clearly resolved (Figure 3d). Nanobelt I exhibits a FWHM of nearly  $16\text{ cm}^{-1}$ , while nanobelt II exhibits a FWHM of nearly  $13\text{ cm}^{-1}$ . It is known that the phonon confinement in nanoscale systems causes broadening of the Raman bands. It has been demonstrated that the Raman bands of ZnO nanocrystals are broader and asymmetrical compared to those of bulk ZnO crystals.<sup>35</sup> Apart from the confinement effects, the broadening of the peaks can also occur due to the oxygen deficiency and residual stresses.<sup>36</sup> To our knowledge, the dependence of the width of the  $E_2$  band on the orientation of the  $c$ -axis is a novel feature never observed earlier, the origin of which remains unclear and needs further investigation.

Apart from the intensity of  $A_1$ -TO mode and width of the  $E_2$  band, the intensity of the Raman signal from the silicon substrate is modulated due to the presence of the nanobelt (Figure 3e). We observed that the Raman signal from silicon substrate is either suppressed or enhanced depending on the orientation of the ZnO belt. The Si Raman signal is enhanced (higher the background) in the case of the nanobelt I, while the same

is suppressed (lower compared to the background) in the case of the nanobelt II (Figure 3e).

The apparent enhancement and suppression of the Si signal can be explained by passive waveguiding properties of the ZnO nanostructures.<sup>37</sup> In fact, the ZnO nanobelt lying on the substrate can be considered as a waveguide composed of three dielectric layers: cladding (air), nanobelt (ZnO), and substrate ( $\text{SiO}_2$ ) (Figure 3f). As the refractive index of the ZnO nanobelt ( $n = 2$ ) is higher than the refractive index of both cladding and substrate, light can be guided. Huang *et al.* have demonstrated UV lasing in vertically oriented ZnO nanowires, with each wire forming a Fabry–Perot resonator bound by reflecting (0001) facets (in the  $c$ -direction).<sup>7</sup>

Even more recently, using spatially resolved luminescence spectroscopy, it has been demonstrated that the light is emitted primarily at both ZnO wire ends due to its waveguiding nature.<sup>38</sup> In the present case, the incident light is either transmitted to the substrate (below the critical angle) through the ZnO nanobelt or guided along the nanobelt (over the critical angle) to exit at different facet (Figure 3f). On the other hand, the scattered light from the substrate is either transmitted through the ZnO belt or guided along the nanobelt to exit at a different facet. Both the effects combined result in either suppression or enhancement of the silicon Raman band when the light is perpendicular and parallel to the  $c$ -axis, respectively.

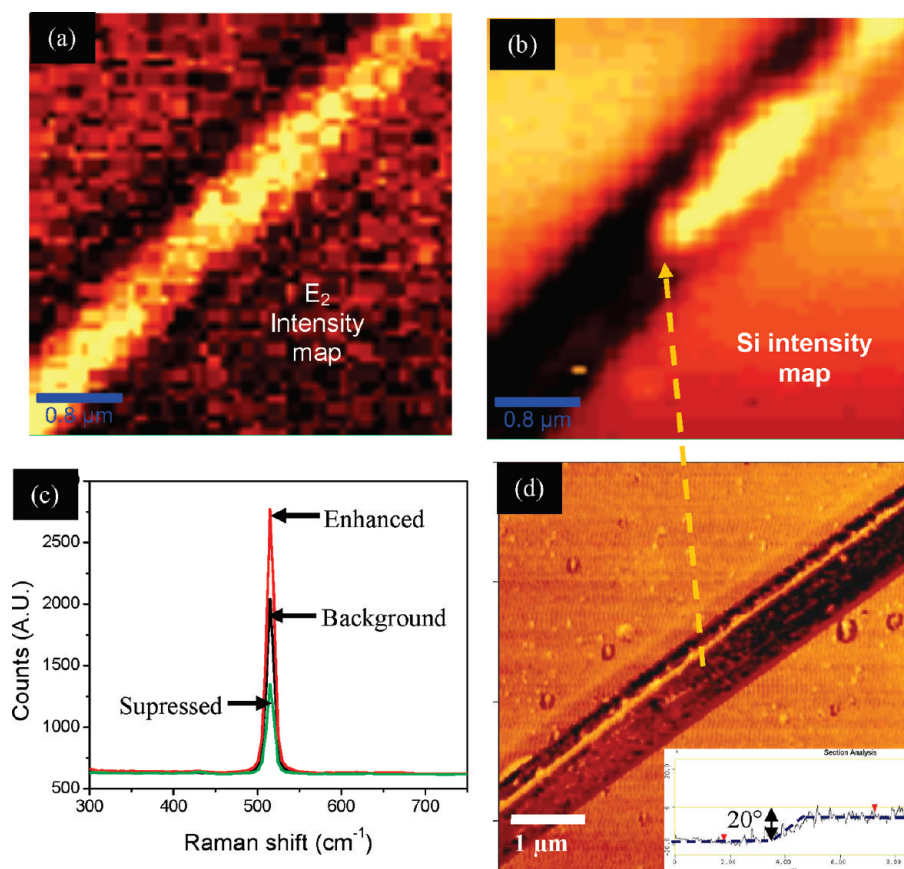


**Figure 5.** Raman intensity map of the (a)  $E_2$  mode of the nanobelt. (b) Silicon band at  $520\text{ cm}^{-1}$ . (c) Raman spectra showing the silicon band at various locations highlighting the intensity variation. (d) AFM phase image showing the ZnO nanobelt with distinct phase contrast between the upper and lower half. Inset shows the cross section along the length of the belt revealing a transition of about  $20^\circ$ . The arrow highlights the location of the change of the crystal orientation in the nanobelt.

In the examples demonstrated so far, the nanobelts grown by vapor deposition are in intimate contact with the silicon surface. We have also performed confocal Raman microscopy on ZnO nanobelts freely suspended across polystyrene micropattern on silicon substrate (Figure 4a). The periodicity of the polystyrene pattern was  $10\ \mu\text{m}$  with a line width of  $7\ \mu\text{m}$  and a thickness of  $500\ \text{nm}$ . Figure 4b shows the intensity map of  $E_2$  band, which is relatively uniform along the length of the nanobelt. Figure 4c,d shows the intensity map of silicon and the  $\text{C}=\text{C}$  stretching of polystyrene, respectively. The thin polystyrene layer acts as a dielectric waveguide (higher refractive index compared to the surrounding air) which enhances the Raman signal from the silicon substrate (Figure 4c). On the other hand, an apparent suppression of the silicon signal is observed at the ZnO nanobelt region. Similar suppression of the polystyrene signal is also observed in the ZnO nanobelt region (Figure 4d). It is clear that the Raman signal from the substrate is suppressed by the ZnO in both of the cases (presence of and absence of direct contact). The suppression of the signal further confirms the waveguiding of the Raman scattered light from the layers underneath the ZnO nanobelts.

The waveguiding of the scattered light from the substrate can be employed to identify the sharp reorientations of the crystal planes in the ZnO nanostructures associated with a defect in crystal growth. In fact, Figure 5a shows the  $E_2$  intensity map of a ZnO nanobelt on a silicon substrate, which is uniform along the length of the belt. On the contrary, the Raman scattering from the silicon substrate exhibits an abrupt change along the length of the nanobelt (Figure 5b). Within the probed length of the nanobelt, the top portion of the nanobelt exhibits an enhancement of the silicon substrate Raman signal replaced by suppression at the bottom portion. From the discussion above, it can be concluded that the areas exhibiting enhancement correspond to the  $c$ -axis perpendicular to the substrate and suppressed areas corresponding to the  $c$ -axis parallel to the substrate. Figure 5c shows the representative Raman spectra from the enhanced, suppressed, and background (reference) areas of the nanowires. The intensity in the enhanced areas is nearly two times higher compared to that of the background areas, which in turn is two times higher compared to the suppressed signal.

AFM analysis of this area of the nanobelt confirmed a transition of the crystal orientation along the long

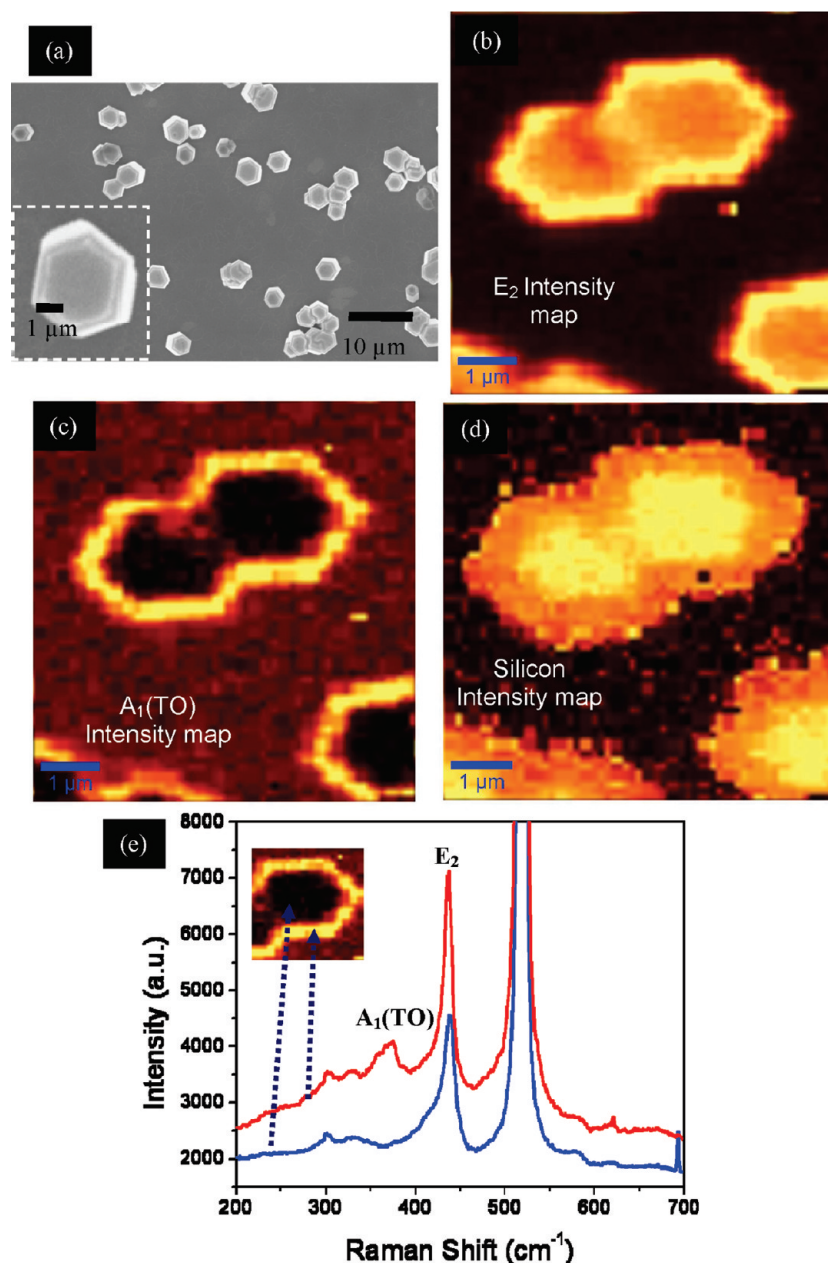


Figure 6. (a) SEM image of vertically grown ZnO nanorods. Intensity map of the of the vertical nanorods (b)  $E_2$  band, (c)  $A_1(\text{TO})$  band, (d) Si band. (e) Raman spectra from the two different regions (shown in the image) of the vertical nanorod.

axis (Figure 5d). While the topography shows no significant changes (not shown here), the phase image shows the presence of the transversal defect and a clear contrast between the two regions in the phase tapping mode (nearly  $20^\circ$ ) (see Figure 5d and longitudinal section as inset). The change in the phase in light tapping is due to the varying interaction between the tip and the crystal facet of the nanobelt. It is known that the  $c$ -planes of the ZnO belts are polar surfaces with either positively charged Zn or negatively charged oxygen ions. The negative charge on the native silicon oxide of the AFM tip is either attracted or repelled from the polar surface of the ZnO nanobelt. On the other hand, nonpolar planes of the ZnO nanobelt exhibit no signifi-

cant electrostatic interaction with the AFM tip, and thus change in the facet orientation must result in significant change in phase contrast as is indeed observed in the AFM image.

Finally, we have investigated the applicability of this approach for vertically grown ZnO nanorods on substrates with Z1 peptide (see Experimental Section for details). The ZnO1 and Z1 peptides have been previously employed to grow a variety of nanostructures such as nanorods and nanoplates.<sup>39,40</sup> Bioassisted growth of ZnO nanostructures implemented here eases growth requirement by enabling their growth in milder conditions and on arbitrary substrates.<sup>41</sup> Previous experiments comparing peptide-assisted growth on dif-

ferent surfaces have shown that the peptide adsorbs in higher concentration on hydrophobic surfaces. Thus polystyrene was chosen to provide a smooth hydrophobic surface for the adsorption of the Z1 peptide and growth of vertically oriented ZnO nanorods (Figure 6a).

The top surface of the nanorods comprises two crystal facets, as can be seen from the SEM image (Figure 6a). The intensity of the  $E_2$  band of the Raman spectra for these structures is uniform over the entire top surface of the nanorods except for the abrupt changes at the edges (Figure 6b). The intensity map of the  $A_1(\text{TO})$  mode exhibits a clear contrast between the two different planes, suggesting that the plane at the center is  $(0001)/(000\bar{1})$  and the edges are  $(2\bar{1}\bar{1}0)/(01\bar{1}0)$  (Figure 6c). The intensity of the silicon substrate shows the expected waveguiding signature: significantly enhanced signal at  $(0001)$  plane and suppressed intensity at the other plane (Figure 6d).

## CONCLUSIONS

In conclusion, we have demonstrated high-resolution confocal Raman microscopy as a nondestructive

technique for fast, unambiguous, and universal identification of the localized crystal orientation of individual ZnO nanostructures. The two important features in the Raman spectra of ZnO which clearly distinguish the  $c$ -axis are the intensity of  $A_1(\text{TO})$  band and the width of the  $E_2$  band. Apart from these two features, the orientation-dependent waveguiding of the Raman scattered signal from the substrate (enhanced parallel to the  $c$ -axis and suppression perpendicular to the  $c$ -axis) has also been revealed.

These features of the Raman bands of the ZnO nanostructures can be extremely powerful for the *in situ* identification of orientation of ZnO nanostructures employed in a converse piezoelectric actuator directly in an assembled state as was discussed elsewhere.<sup>42</sup> While the study here is focused on ZnO nanostructures, the general features, Raman bands and the waveguiding effect, described here are equally applicable to other wurtzite-type nanostructures. The approach suggested here might serve as a universal tool for the versatile characterization of GaN, ZnS, and CdSe from the wurtzite family, which are utilized in optoelectronics, lasing, and piezotronic devices.

## EXPERIMENTAL SECTION

The ZnO nanobelts lying on the silicon wafer were grown by a vapor–solid process and peptide-assisted wet chemistry growth as described in detail earlier.<sup>43</sup> ZnO powders were placed at the center of an alumina tube with a collecting alumina substrate downstream. The alumina tube was inserted in a horizontal tube furnace, which was later heated to 1475 °C, and the synthesis lasted for 2 h. The as-grown product on the alumina substrate contained an entangled mass of ZnO nanobelts, which was gently brushed and collected for further analysis. The process results in sparsely dispersed and randomly oriented ZnO belts.

The vertically aligned peptide-assisted nanorods were grown using a solution-based approach employing a Z1 peptide (GLH-VMHKVAPPRGGGC).<sup>39</sup> The sequence of the Z1 peptide contained two histidine residues, and amino acids coordinate with  $\text{Zn}^{2+}$  ions within the active sites of several enzymes.<sup>44,45</sup> A thin layer of polystyrene (15 nm) was spin coated on a silicon wafer. The peptide (10 mg/mL) was dropped onto the polystyrene layer, left to adsorb to the polymer layer for 15 min, and spun dry at 6000 rpm. After spinning, the thickness of the peptide layer was measured with ellipsometry to be 3.5 nm, a thick layer for a peptide considering the mass of 1616 Da. The resulting surface was smooth with an rms of 0.26 nm over a  $1\ \mu\text{m} \times 1\ \mu\text{m}$  area.

The sample was placed in a vial of  $\text{Zn}(\text{NO}_3)_2$  and HMTA (1,3-hexamethylenetetraamine), both at 0.1 M concentrations at a 1:1 ratio. The sample was held at room temperature for 24 h, and then the vial was put into an oven at 65 °C for 24 h. The vertically aligned zinc oxide nanorods were gently rinsed with water and dried under flowing nitrogen air.

Morphological studies of grown ZnO nanostructures have been performed with a LEO 1530 field emission scanning electron microscopy (SEM). Samples for (transmission electron microscopy) TEM were prepared by gently touching the indexed copper grids to the substrate with ZnO nanobelts. TEM and electron diffraction measurements were carried out at 200 kV using a Hitachi HF2000 microscope. Following the TEM measurements, Raman measurements were performed on the same ZnO nanobelts with known crystal plane orientations. Atomic force microscopy (AFM) was performed on the ZnO nanobelts using a Dimension 3000 AFM (Digital Instruments) in tapping mode.<sup>46,47</sup>

Raman measurements were performed using a Witec (Alpha 300R) confocal Raman microscope using  $\text{Ar}^+$  ion laser ( $\lambda = 514.5$

nm) as an excitation source. The intensity of the excitation source was fixed at 4 mW. Raman imaging of the ZnO nanostructures was performed using a 600 grooves/mm grating with a resolution of  $\sim 3\ \text{cm}^{-1}$ . The typical imaging was performed at a resolution of  $50 \times 50$  pixels unless mentioned otherwise, with each spectra collected for 0.7 s. The short collection interval used here eliminates the possibility of laser-induced heating. The individual spectra were collected locally over a longer time using 1800 grooves/mm grating with a resolution of about  $0.5\ \text{cm}^{-1}$ . The sample is scanned with a piezoelectric stage with a nominal accuracy of about 1 nm in the lateral directions. Focusing on the sample was done with a  $100\times$  objective (Olympus MPL 100X-NA = 0.90).

**Acknowledgment.** We would like to thank K. Bergman for technical assistance in the preparation of the vertically aligned nanorods. This work was supported by funding provided by the Air Office of Scientific Research and Air Force Research laboratory.

## REFERENCES AND NOTES

- Wang, Z. L. Characterizing the Structure and Properties of Individual Wire-like Nanoentities. *Adv. Mater.* **2000**, *12*, 1295–1298.
- Xia, Y.; Yang, P.; Sun, Y.; Wu, Y.; Mayers, B.; Gates, B.; Yin, Y.; Kim, F.; Yan, H. One-Dimensional Nanostructures: Synthesis, Characterization, and Applications. *Adv. Mater.* **2003**, *15*, 353–389.
- Pan, Z.; Budai, J. D.; Dai, Z. R.; Liu, W.; Paranthaman, M. P.; Dai, S. Zinc Oxide Microtowers by Vapor Phase Homoepitaxial Regrowth. *Adv. Mater.* **2009**, *21*, 890–896.
- Ko, H.; Singamaneni, S.; Tsukruk, V. V. Nanostructured Surfaces and Assemblies as SERS Media. *Small* **2008**, *4*, 1576–1599.
- Law, M.; Sirbuly, D. J.; Johnson, J. C.; Goldberger, J.; Saykally, R. J.; Yang, P. Nanoribbon Waveguides for Subwavelength Photonics Integration. *Science* **2004**, *305*, 1269–1273.
- Tong, L.; Gattass, R. R.; Ashcom, J. B.; He, S.; Lou, J.; Shen, M.; Maxwell, I.; Mazur, E. Subwavelength-Diameter Silica Wires for Low-Loss Optical Wave Guiding. *Nature* **2003**, *426*, 816–819.

7. Huang, M. H.; Mao, S.; Feick, H.; Yan, H.; Wu, Y.; Kind, H.; Weber, E.; Russo, R.; Yang, P. Room-Temperature Ultraviolet Nanowire Nanolasers. *Science* **2001**, *292*, 1897–1899.
8. Agarwal, R.; Barrelet, C. J.; Lieber, C. M. Lasing in Single Cadmium Sulfide Nanowire Optical Cavities. *Nano Lett.* **2005**, *5*, 917–920.
9. Duan, X.; Huang, Y.; Agarwal, R.; Lieber, C. M. Single-Nanowire Electrically Driven Lasers. *Nature* **2003**, *421*, 241–245.
10. Zou, B. S.; Liu, R. B.; Wang, F. F.; Pan, A. L.; Cao, L.; Wang, Z. L. Lasing Mechanism of ZnO Nanowires/Nanobelts at Room Temperature. *J. Phys. Chem. B* **2006**, *110*, 12865–12873.
11. Wang, Z. L.; Song, J. H. Piezoelectric Nanogenerators Based on Zinc Oxide Nanowire Arrays. *Science* **2006**, *312*, 242–246.
12. Wang, X. D.; Song, J. H.; Liu, J.; Wang, Z. L. Direct-Current Nanogenerator Driven by Ultrasonic Waves. *Science* **2007**, *316*, 102–105.
13. Cole, J. J.; Wang, X.; Knuesel, R. J.; Jacobs, H. O. Patterned Growth and Transfer of ZnO Micro and Nanocrystals with Size and Location Control. *Adv. Mater.* **2008**, *20*, 1474–1478.
14. Kouklin, N. Cu-Doped ZnO Nanowires for Efficient and Multispectral Photodetection Applications. *Adv. Mater.* **2008**, *20*, 2190–2194.
15. Wang, X. D.; Zhou, J.; Song, J. H.; Liu, J.; Xu, N. S.; Wang, Z. L. Piezoelectric Field Effect Transistor and Nanoforce Sensor Based on a Single ZnO Nanowire. *Nano Lett.* **2006**, *6*, 2768–2772.
16. Lao, C. S.; Kuang, Q.; Wang, Z. L.; Park, C. M.; Deng, Y. Polymer-Functionalized Piezoelectric-FET as Humidity/Chemical Nanosensors. *Appl. Phys. Lett.* **2007**, *90*, 262107.
17. He, J. H.; Hsin, C. L.; Liu, J.; Chen, L. J.; Wang, Z. L. Piezoelectric Gated Diode of a Single ZnO Nanowire. *Adv. Mater.* **2007**, *19*, 781–784.
18. He, J. H.; Lin, Y. H.; McConney, M. E.; Tsukruk, V. V.; Wang, Z. L.; Bao, G. Enhancing UV Photoconductivity of ZnO Nanobelt by Polyacrylonitrile Functionalization. *J. Appl. Phys.* **2007**, *102*, 084303.
19. He, J.-H.; Singamaneni, S.; Ho, C. H.; Lin, Y.-H.; McConney, M. E.; Tsukruk, V. V. A Thermal Sensor and Switch Based on a Plasma Polymer/ZnO Suspended Nanobelt Bimorph Structure. *Nanotechnology* **2009**, *20*, 065502.
20. Ding, Y.; Wang, Z. L. Structure Analysis of Nanowires and Nanobelts by Transmission Electron Microscopy. *J. Phys. Chem. B* **2004**, *108*, 12280–12291.
21. Rao, A. M.; Richter, E.; Bandow, S.; Chase, B.; Eklund, P. C.; Williams, K. A.; Fang, S.; Subbaswamy, K. R.; Menon, M.; Thess, A.; Smalley, R. E.; Dresselhaus, G.; Dresselhaus, M. S. Diameter-Selective Raman Scattering from Vibrational Modes in Carbon Nanotubes. *Science* **1997**, *275*, 187–191.
22. Bachilo, S. M.; Strano, M. S.; Kittrell, C.; Hauge, R. H.; Smalley, R. E.; Weisman, R. B. Structure-Assigned Optical Spectra of Single-Walled Carbon Nanotubes. *Science* **2002**, *298*, 2361–2366.
23. Jiang, C.; Ko, H.; Tsukruk, V. V. Strain-Sensitive Raman Modes of Carbon Nanotubes in Deflecting Freely Suspended Nanomembranes. *Adv. Mater.* **2005**, *17*, 2127–2131.
24. Atashbar, M. Z.; Singamaneni, S. Comparative Studies of Temperature Dependence of G-Band Peak in Single Walled Carbon Nanotube and Highly Oriented Pyrolytic Graphite. *Appl. Phys. Lett.* **2005**, *86*, 123112.
25. Ko, H.; Pikus, Y.; Jiang, C.; Jauss, A.; Hollricher, O.; Tsukruk, V. V. High-Resolution Raman Microscopy of Curled Carbon Nanotubes. *Appl. Phys. Lett.* **2004**, *85*, 2598–2600.
26. Jiang, C.; Lio, W. Y.; Tsukruk, V. V. Surface Enhanced Raman Scattering Monitoring of Chain Alignment in Freely Suspended Nanomembranes. *Phys. Rev. Lett.* **2005**, *95*, 115503.
27. Bliznyuk, V.; Singamaneni, S.; Sanford, R. L.; Chiappetta, D.; Crooker, B.; Shibaev, P. V. Matrix Mediated Alignment of Single Wall Carbon Nanotubes in Polymer Composite Films. *Polymer* **2006**, *47*, 3915–3921.
28. Pauzauskie, P. J.; Talaga, D.; Seo, K.; Yang, P.; Lagugné-Labarthe, F. Polarized Raman Confocal Microscopy of Single Gallium Nitride Nanowires. *J. Am. Chem. Soc.* **2005**, *127*, 17146–17147.
29. Livneh, T.; Zhang, J.; Cheng, G.; Moskovits, M. Polarized Raman Scattering from Single GaN Nanowires. *Phys. Rev. B* **2006**, *74*, 035320.
30. Tripathy, S.; Chua, S. J.; Chen, P.; Miao, Z. L. Micro-Raman Investigation of Strain in GaN and Al<sub>1-x</sub>Ga<sub>x</sub>N/GaN Heterostructures Grown on Si(111). *J. Appl. Phys.* **2002**, *92*, 3503–3510.
31. Cong, G. W.; Wei, H. Y.; Zhang, P. F.; Peng, W. Q.; Wu, J. J.; Liu, X. L.; Jiao, C. M.; Hu, W. G.; Zhu, Q. S.; Wang, Z. G. One-Step Growth of ZnO From Film to Vertically Well-Aligned Nanorods and the Morphology-Dependent Raman Scattering. *Appl. Phys. Lett.* **2005**, *87*, 231903.
32. Ozgur, U.; Alivov, Y.; Liu, C.; Teke, A.; Reshchikov, M. A.; Dogan, S.; Avrutin, V.; Cho, S. J.; Morkoc, H. A Comprehensive Review of ZnO Materials and Devices. *J. Appl. Phys.* **2005**, *98*, 041301.
33. Wang, Z. L. Oxide Nanobelts and Nanowires—Growth, Properties and Applications. *J. Nanosci. Nanotechnol.* **2008**, *8*, 27–55.
34. Pan, Z. W.; Dai, Z. R.; Wang, Z. L. Nanobelts of Semiconducting Oxides. *Science* **2001**, *291*, 1947–1949.
35. Du, Y.; Zhang, M. S.; Hong, J.; Shen, Y.; Chen, Q.; Yin, Z. Structural and Optical Properties of Nanophase Zinc Oxide. *Appl. Phys. A* **2003**, *76*, 171–176.
36. Ng, H. T.; Chen, B.; Li, J.; Han, J.; Meyyappan, M.; Wu, J.; Li, S. X.; Haller, E. E. Optical Properties of Single-Crystalline ZnO Nanowires on *m*-Sapphire. *Appl. Phys. Lett.* **2003**, *82*, 2023–2025.
37. Djuricic, A. B.; Leung, Y. H. Optical Properties of ZnO Nanostructures. *Small* **2006**, *2*, 944–961.
38. Rühle, S.; van Vugt, L. K.; Li, H.-Y.; Keizer, N. A.; Kuipers, L.; Vanmaekelbergh, D. Nature of Sub-Band Gap Luminescent Eigenmodes in a ZnO Nanowire. *Nano Lett.* **2008**, *8*, 119–123.
39. Umetsu, M.; Mizuta, M.; Tsumoto, K.; Ohara, S.; Takami, S.; Watanabe, H.; Kumagai, I.; Adschiri, T. Bioassisted Room-Temperature Immobilization and Mineralization of Zinc Oxide—The Structural Ordering of ZnO Nanoparticles into a Flower-Type Morphology. *Adv. Mater.* **2005**, *17*, 2571–2575.
40. Tomczak, M. M.; Gupta, M. K.; Drummy, L. F.; Rozenzhak, S. M.; Naik, R. R. Morphological Control and Assembly of Zinc Oxide Using a Biotemplate. *Acta Biomater.* **2009**, *5*, 876–882.
41. Weintraub, B.; Chang, S.; Singamaneni, S.; Han, W. H.; Choi, Y. J.; Bae, J.; Kirkham, M.; Tsukruk, V. V.; Deng, Y. Density-Controlled, Solution-Based Growth of ZnO Nanorod Arrays via Layer-by-Layer Polymer Thin Films for Enhanced Field Emission. *Nanotechnology* **2008**, *19*, 435302.
42. Hu, Y.; Gao, Y.; Singamaneni, S.; Tsukruk, V. V.; Wang, Z. L. Converse Piezoelectric Effect Induced Transverse Deflection of a Free-Standing ZnO Microbelt. *Nano Lett.* **2009**, *9*, 2661–2665.
43. Pan, Z. W.; Dai, Z. R.; Wang, Z. L. Nanobelts of Semiconducting Oxides. *Science* **2001**, *291*, 1947–1949.
44. Fraústo da Silva, J. J. R.; Williams, R. J. P. *The Biological Chemistry of the Elements*; Oxford University Press: New York, 2001.
45. Dickerson, M. B.; Sandhage, K. H.; Naik, R. R. Protein- and Peptide-Directed Syntheses of Inorganic Materials. *Chem. Rev.* **2008**, *108*, 4935–4978.
46. Tsukruk, V. V.; Reneker, D. H. Scanning Probe Microscopy of Organic and Polymeric Films: From Self-Assembled Monolayers to Composite Multilayers. *Polymer* **1995**, *36*, 1791–1808.
47. Tsukruk, V. V. Scanning Probe Microscopy of Polymer Surfaces. *Rubber Chem. Technol.* **1997**, *70*, 430–467.